



# Free-standing and porous hierarchical nanoarchitectures constructed with cobalt cobaltite nanowalls for supercapacitors with high specific capacitances

Yuanhua Xiao<sup>a,b</sup>, Aiqin Zhang<sup>a,b</sup>, Shaojun Liu<sup>a</sup>, Jihong Zhao<sup>a</sup>, Shaoming Fang<sup>a</sup>, Diansheng Jia<sup>b</sup>, Feng Li<sup>a,b,\*</sup>

<sup>a</sup> College of Materials and Chemical Engineering, State Laboratory of Surface and Interface Science and Technology, Zhengzhou University of Light Industry, Zhengzhou 450002, PR China

<sup>b</sup> Institute of Applied Chemistry, Xinjiang University, Urumqi 830046, PR China

## H I G H L I G H T S

- Free-standing and porous Co<sub>3</sub>O<sub>4</sub> nanowalls have been synthesized on large scale.
- The step-by-step decomposition of precursor generates porous nanoarchitectures.
- Supercapacitors made with the materials exhibit excellent performances.

## A R T I C L E I N F O

### Article history:

Received 13 February 2012

Received in revised form

19 May 2012

Accepted 12 July 2012

Available online 24 July 2012

### Keywords:

Cobalt cobaltite

Porous nanoarchitecture

Nanowalls

Supercapacitors

Electrochemical property

## A B S T R A C T

Free-standing and porous hierarchical nanoarchitectures constructed with cobalt cobaltite (Co<sub>3</sub>O<sub>4</sub>) nanowalls have been successfully synthesized in large scale by calcining three dimensional (3D) hierarchical nanostructures consisting of single crystalline cobalt carbonate hydroxide hydrate – Co(CO<sub>3</sub>)<sub>0.5</sub>(OH)·0.11H<sub>2</sub>O nanowalls prepared with a solvothermal method. The step-by-step decomposition of the precursor can generate porous Co<sub>3</sub>O<sub>4</sub> nanowalls with BET surface area of 88.34 m<sup>2</sup> g<sup>−1</sup>. The as-prepared Co<sub>3</sub>O<sub>4</sub> nanoarchitectures show superior specific capacitance to the most Co<sub>3</sub>O<sub>4</sub> supercapacitor electrode materials to date. After continuously cycled for 1000 times of charge–discharge at 4 A g<sup>−1</sup>, the supercapacitors can retain ca 92.3% of their original specific capacitances. The excellent performances of the devices can be attributed to the porous and hierarchical 3D nanostructure of the materials.

© 2012 Elsevier B.V. All rights reserved.

## 1. Introduction

Supercapacitors, as one class of energy storage devices, have attracted extensive attention, because of their highly improved power density in recent years, long cycle life, short charge time, and thus one of the potential options in tackling the energy and environmental challenges emerging in accompanying with the rapid developments of modern society [1–3]. According to the fundamental mechanisms of capacitance, the devices can be divided into 1) electrical double-layer capacitors (EDLCs), in which the

\* Corresponding author. College of Materials and Chemical Engineering, State Laboratory of Surface and Interface Science and Technology, Zhengzhou University of Light Industry, Zhengzhou 450002, PR China. Tel.: +86 188 3802 9203; fax: +86 371 6355 6510.

E-mail addresses: [fengli@zzuli.edu.cn](mailto:fengli@zzuli.edu.cn), [lifeng696@yahoo.com](mailto:lifeng696@yahoo.com) (F. Li).

capacitance arises from charge separation at the electrode/electrolyte interface, and 2) electrochemical capacitors (ECs) where redox reactions take place reversibly [2]. To date, carbon-related materials have been widely utilized as building blocks to construct electrodes for EDLCs due to their good processing ability, large surface area/porosity, good cycle life, and low cost [4,5]. However, the devices fabricated suffer from their relative low capacity in storing charge [5]. In contrast, the ECs made with transition metal oxides have drawn extensive research attention for their improved specific capacitances through tuning the microstructures of materials [6–10]. Supercapacitors made with RuO<sub>2</sub> materials, for instance, show excellent performances with a specific capacitance as high as 1580 F g<sup>−1</sup> [11]. However, the practical applications of supercapacitors fabricated with RuO<sub>2</sub>-based materials are hindered for their high cost and the difficulty in accessing the materials. Toward the end of commercializing ECs in applications such as hybrid electric vehicles and energy management

systems, diverse efforts have thus focused on low-cost transition metal oxide materials including  $\text{Fe}_2\text{O}_3$  [12],  $\text{MnO}_2$  [13],  $\text{WO}_3/\text{MoO}_3$  [9,14],  $\text{Co}_3\text{O}_4$  [15], and their composites [6,16–20] for exploring alternative pathways to tailor the functionalities of electrode materials and construct supercapacitors with enhanced energy and power densities.

Cobalt cobaltite ( $\text{Co}_3\text{O}_4$ ) is one of the important transition metal oxides and has been utilized in designing and fabricating catalysts [21], biosensors [22], field emitters [23] and Li-batteries [24]. It is also a promising candidate for constructing supercapacitors, because of their relative low environmental footprint, low cost and high specific capacitance of  $3560 \text{ F g}^{-1}$  in theory [15,25–36]. However, the realized specific capacitances of the devices are still much lower than the value expected so far. Because the capacitance performances of supercapacitors are mainly dominated by the electron transportation and ion diffusion in the electrodes [1,2], extensive efforts have therefore focused on controlling the nanostructures of  $\text{Co}_3\text{O}_4$  nanocrystals for improving the kinetics of ion and electron transportation in the energy storage devices [37,38].  $\text{Co}_3\text{O}_4$  materials with different structures including nanoparticles [15], nanowalls [26], nanowires [34], nanorods [39], nanotubes [40], nanoboxes [41], polyhedrons [42] and hierarchical microspheres [43] have been already synthesized successfully with different methods. Novel supercapacitors with excellent performances have been fabricated with porous layered parallel folding  $\text{Co}_3\text{O}_4$  nanostructures ( $202.5 \text{ F g}^{-1}$  at  $1 \text{ A g}^{-1}$ ) [27], urchin-like hierarchical  $\text{Co}_3\text{O}_4$  nanostructures ( $536 \text{ F g}^{-1}$  at  $4 \text{ A g}^{-1}$ ) [33], mesoporous  $\text{Co}_3\text{O}_4$  nanoparticles ( $401 \text{ F g}^{-1}$  at  $0.5 \text{ A g}^{-1}$ ) [35],  $\text{Co}_3\text{O}_4$  aerogels ( $>600 \text{ F g}^{-1}$ ) [36],  $\text{Co}_3\text{O}_4$  nanotubes ( $574 \text{ F g}^{-1}$  at  $0.1 \text{ A g}^{-1}$ ) [40] and mesoporous  $\text{Co}_3\text{O}_4$  monolayer ( $345 \text{ F g}^{-1}$  at  $4 \text{ A g}^{-1}$ ) [44]. Recently, it was found that  $\text{Co}_3\text{O}_4$  nanoparticles show specific capacitance of  $776 \text{ F g}^{-1}$  at current density of  $12 \text{ A g}^{-1}$  [15], compared to hollow  $\text{Co}_3\text{O}_4$  nanowire arrays of  $599 \text{ F g}^{-1}$  at  $2 \text{ A g}^{-1}$  [25]. In addition, the ECs fabricated with  $\text{Co}_3\text{O}_4$  nanonets with porous 2D structure exhibit high specific capacitance of  $1090 \text{ F g}^{-1}$  at a scan rate of  $10 \text{ mV s}^{-1}$ , while the materials are limited for their working stability to some extent. The specific capacitance of the ECs fabricated with  $\text{Co}_3\text{O}_4$  nanonets is comparable to that of the devices made with  $\text{RuO}_2$  materials [45,46]. Therefore the electrochemical properties of  $\text{Co}_3\text{O}_4$  nanocrystals have been investigated extensively [24,28,42,47–50].

Herein we report free-standing and porous hierarchical nanoarchitectures constructed with  $\text{Co}_3\text{O}_4$  nanowalls and their electrochemical properties. After yielded in solvothermal reaction, the single crystalline precursor –  $\text{Co}(\text{CO}_3)_{0.5}(\text{OH}) \cdot 0.11\text{H}_2\text{O}$  hierarchical nanoarchitectures composed of nanowalls, decompose to form free-standing and porous  $\text{Co}_3\text{O}_4$  nanoarchitectures under calcination by releasing  $\text{H}_2\text{O}$  and  $\text{CO}_2$  gases from the system. The as-prepared materials can be utilized as building blocks to make supercapacitors with excellent pseudocapacitive performances including specific capacitance and stability. The results indicate that the free-standing and porous  $\text{Co}_3\text{O}_4$  nanoarchitectures are promising candidates for designing energy storage devices.

## 2. Experimental section

All of the reagents were analytically pure, and purchased from Shanghai Chemical Industrial Co. Ltd. (Shanghai, China), and used without further purification.

### 2.1. Sample preparation

In a typical synthesis, Cobalt nitrate hexahydrate ( $\text{Co}(\text{NO}_3)_2 \cdot 6\text{H}_2\text{O}$ ) (1.455 g, 5 mmol) were first dissolved in deionized water (15 mL) and ethylene glycol (EG) (25 mL) to form a homogeneous

solution under continuous magnetic stirring. Then, urea ( $\text{NH}_2\text{CONH}_2$ ) (0.01 g, 0.17 mmol) was added into the above solution and the mixture was stirred for another 20 min to obtain homogeneous solution, which was transferred into a Teflon-lined autoclave with a volume of 40 mL. The autoclave was heated in a temperature preset oven at  $180^\circ\text{C}$  for 20 h. After cooled down to room temperature naturally, the precipitates were collected by centrifugation and rinsed with deionized water and ethanol for 5 times each, and dried in an oven at  $80^\circ\text{C}$  for 12 h to get red powders of precursor. Finally, the samples were calcined in a muffle furnace at a temperature of  $400^\circ\text{C}$  for 2 h in air, and then cooled to room temperature. The resulting black powders of the final products were collected for the characterization and applications.

### 2.2. Sample characterizations

The composition of the precursor and the final products were measured by powder X-ray diffraction (XRD) with a D/max 2550 V X-ray diffractometer (Rigaku, Tokyo, Japan) with monochromatized  $\text{Cu K}\alpha$  incident radiation ( $\lambda = 1.54056 \text{ \AA}$ ; scanning rate:  $0.04^\circ \text{ s}^{-1}$  in the range of  $10^\circ$ – $80^\circ$ ). The morphologies and sizes of the as-prepared samples were analyzed with Field Emission Scanning Electron Microscopy (FESEM, JSM-7001F) and Transmission Electron Microscopy (TEM, JEM-2100 operated at 200 kV). The specific surface area and pore size of the materials were measured using a Belsorp-Mini adsorption apparatus (Bel Japan Inc). The pore size distribution was determined using BJH method applied to the desorption branch of adsorption–desorption isotherms. Thermogravimetry (TG) analysis and differential thermal analysis (DTA) was carried out on SDTQ600 thermal analyzer under air atmosphere at temperature ranging from 30 to  $900^\circ\text{C}$  with a heating rate of  $5^\circ\text{C min}^{-1}$ .

### 2.3. Electrochemical properties

Electrochemical studies were carried out in a three-electrode system. A piece of nickel foam mesh coated with freshly prepared  $\text{Co}_3\text{O}_4$  nanoarchitectures, a platinum electrode and a saturated calomel electrode (SCE) were used as working electrode, counter electrode, and reference electrode, respectively. The electrode materials to construct working electrodes were composed of active materials ( $\text{Co}_3\text{O}_4$ , 80 wt%,  $1 \text{ mg cm}^{-2}$ ), conductive material (acetylene carbon black, ATB, 10 wt%) and binder (polytetrafluoroethylene, PTFE, 10 wt%). After the mixture of electrode materials was ground for *ca* 10 min, it was coated onto the surfaces of nickel foam meshes (*ca*  $1 \times 1 \text{ cm}^2$ ). The sheets with electrode materials were first dried at  $100^\circ\text{C}$  for 12 h and then pressed under 10 Mpa to obtain working electrodes. The electrolyte used in the system was aqueous KOH solution ( $6 \text{ mol L}^{-1}$ ). Cyclic voltammogram (CV) and electrochemical impedance spectroscopy (EIS) were measured by a CHI 660D electrochemical workstation. CV tests were done between 0 and 0.5 V (vs. SCE) at scan rates of 5, 10, 20 and  $50 \text{ mV s}^{-1}$ , respectively. The EIS measurements were carried out in the frequency ranging from 0.01 Hz to 100 kHz with an ac perturbation of 5 mV with the help of an impedance spectrum analyzer. Galvanostatic charge/discharge cycle tests were performed on a LAND Cell test system CT2001A (Wuhan, China). The specific capacitances of the supercapacitors can be evaluated from the charge/discharge test together with the following equation (Eq. (1)):

$$C_m = I\Delta t/m\Delta V \quad (1)$$

where  $C_m$  is the specific capacitance of the capacitor ( $\text{F g}^{-1}$ ),  $I$  is the current of the charge/discharge (A), and  $\Delta t$  is the discharging time

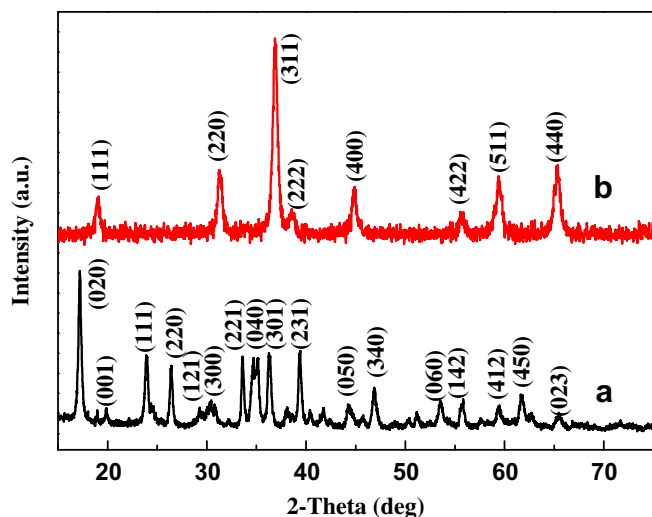


Fig. 1. XRD patterns of (a)  $\text{Co}(\text{CO}_3)_{0.5}(\text{OH}) \cdot 0.11\text{H}_2\text{O}$  precursor and (b)  $\text{Co}_3\text{O}_4$  powders.

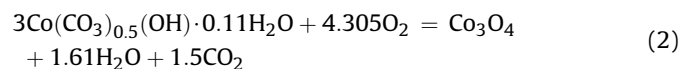
period in seconds for the potential change  $\Delta V$ . The  $m$  is the loaded mass of active materials at the working electrode. All of the working electrodes were activated electrochemically before the electrochemical measurements [51,52].

### 3. Results and discussions

The precursor and final product were first characterized with X-ray diffraction as shown in Fig. 1. The XRD profiles of the precursor (Fig. 1a) can be indexed as orthorhombic cobalt carbonate hydroxide hydrate —  $\text{Co}(\text{CO}_3)_{0.5}(\text{OH}) \cdot 0.11\text{H}_2\text{O}$  with lattice constants of  $a = 0.886$  nm,  $b = 1.012$  nm and  $c = 0.444$  nm (JCPDS Card No. 48-0083). After annealed at  $400^\circ\text{C}$  for 2 h, the precursor has decomposed completely and converted from orthorhombic  $\text{Co}(\text{CO}_3)_{0.5}(\text{OH}) \cdot 0.11\text{H}_2\text{O}$  into cubic  $\text{Co}_3\text{O}_4$  as shown in Fig. 1b. It can be found that all of the diffraction peaks in the XRD profile of the product agree well with the cubic  $\text{Co}_3\text{O}_4$  (JCPDS Card No. 42-1467,  $a = 0.8037$ ). The X-ray diffraction pattern of the material also proves the highly crystalline nature of the materials. There is no any other peaks detected, which indicate its high purity.

The FESEM images as shown in Fig. 2a–c reveals the morphology of the orthorhombic  $\text{Co}(\text{CO}_3)_{0.5}(\text{OH}) \cdot 0.11\text{H}_2\text{O}$  precursor. It can be

observed that large and free-standing 3D nanoarchitectures consisting of nanowalls with edge of  $\text{ca } 62.3$  nm in thicknesses and smooth surfaces of  $\text{ca } 16 \mu\text{m}^2$  in area have been produced successfully in large scale. After annealed at  $400^\circ\text{C}$  for 2 h, the 3D hierarchical structure of the materials is maintained as shown in Fig. 2d–e, while the orthorhombic  $\text{Co}(\text{CO}_3)_{0.5}(\text{OH}) \cdot 0.11\text{H}_2\text{O}$  decomposes to form cubic  $\text{Co}_3\text{O}_4$  and the thickness of the nanowalls shrinks to  $\text{ca } 50.5$  nm. It can be clearly observed that lots of pores have been generated on the surfaces of the  $\text{Co}_3\text{O}_4$  nanowalls (Fig. 2e–f), while the final  $\text{Co}_3\text{O}_4$  products have inherited the 3D hierarchical nanostructure of the precursor. The porous structure of the  $\text{Co}_3\text{O}_4$  nanoarchitectures should be resulted from the decomposition of the  $\text{Co}(\text{CO}_3)_{0.5}(\text{OH}) \cdot 0.11\text{H}_2\text{O}$  precursor and the release of  $\text{H}_2\text{O}$  and  $\text{CO}_2$  from the system (Eq. (2)).



The thermal behaviors of the precursor were further investigated by TG-DTA measurements. The TG-DTA curves (Fig. 3) show that there are two different regions of weight loss in accompanying the increase of temperature. After losing 1.6% of its weight between 30 and  $200^\circ\text{C}$  for the removal of surface water, the precursor first decomposes exothermically at  $331^\circ\text{C}$  with a weight loss of 9.46% for the decomposition of hydroxy group and release of crystalline water from the system (calculated weight loss: 9.38%). Subsequently, the second weight loss of 16.25% takes place at  $408^\circ\text{C}$  exothermically, which can be attributed to the complete decomposition of the carbonate group and the release of  $\text{CO}_2$  from the precursor (calculated weight loss: 21.36%). The TG-DTA results verify that the porous structure of as-prepared  $\text{Co}_3\text{O}_4$  nanoarchitectures has been generated by releasing of  $\text{H}_2\text{O}$  and  $\text{CO}_2$  in accompanying with the step-by-step decomposition of the as-prepared precursor.

The microstructures of the  $\text{Co}(\text{CO}_3)_{0.5}(\text{OH}) \cdot 0.11\text{H}_2\text{O}$  precursor and the porous  $\text{Co}_3\text{O}_4$  nanoarchitectures were further characterized in detail by TEM and SAED. Fig. 4a shows the low magnification TEM image of a piece of representative  $\text{Co}(\text{CO}_3)_{0.5}(\text{OH}) \cdot 0.11\text{H}_2\text{O}$  nanowall with smooth surfaces, which agrees well with the FESEM observations. The high-resolution TEM (HRTEM) analysis of the precursor indicates that the nanowall is single crystalline (Fig. 4b). The measured d-spacings of 0.25 nm correspond to the (040) plane of orthorhombic  $\text{Co}(\text{CO}_3)_{0.5}(\text{OH}) \cdot 0.11\text{H}_2\text{O}$ . Meanwhile, the SAED pattern (inset in Fig. 4b) of the same nanowall further confirms the

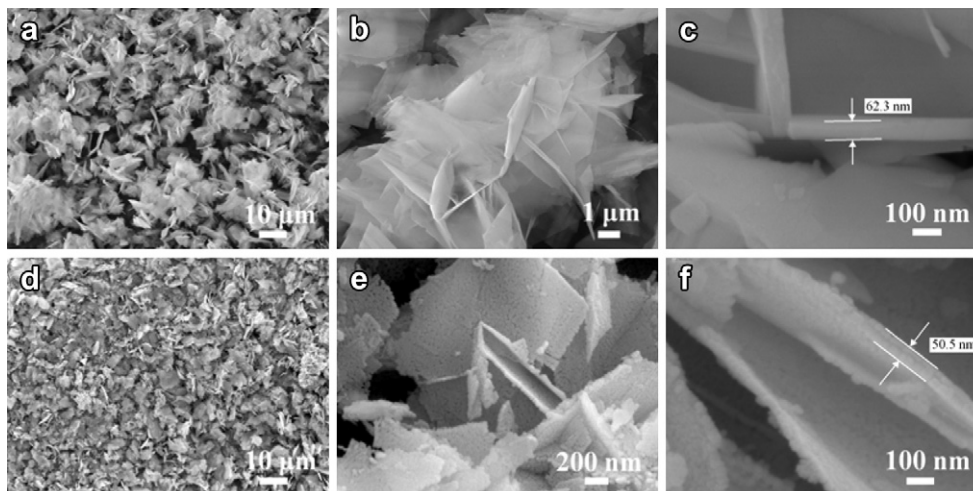


Fig. 2. FESEM images of (a–c)  $\text{Co}(\text{CO}_3)_{0.5}(\text{OH}) \cdot 0.11\text{H}_2\text{O}$  precursor and (d–e)  $\text{Co}_3\text{O}_4$  nanoarchitectures.



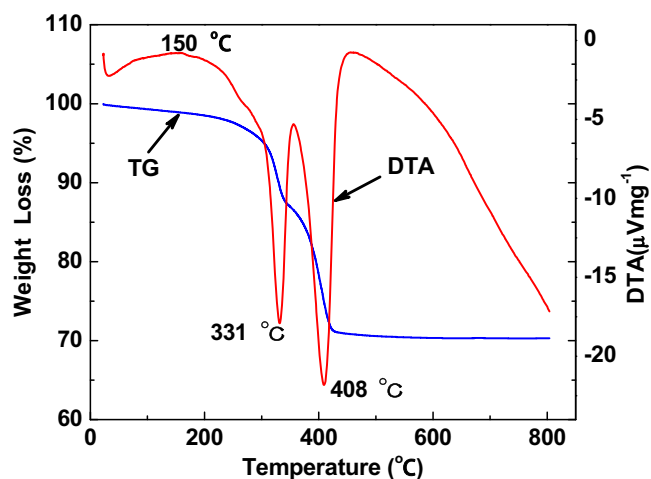


Fig. 3. TG and DTA curves of  $\text{Co}(\text{CO}_3)_{0.5}(\text{OH}) \cdot 0.11\text{H}_2\text{O}$  precursor.

single crystalline feature of the precursor. In contrast, the TEM image of the final  $\text{Co}_3\text{O}_4$  product clearly shows the porous structure of the materials. There are lots of irregular pores of a few to tens of nanometers randomly distributed on the surface of the  $\text{Co}_3\text{O}_4$  nanowall as shown in Fig. 4c. The HRTEM image (Fig. 4d) and SAED pattern (inset in Fig. 4d) of the  $\text{Co}_3\text{O}_4$  nanowall further confirm the polycrystalline feature of the materials. The resolved fringes of 0.28 nm correspond to the (220) facet of cubic  $\text{Co}_3\text{O}_4$  crystal.

To evaluate the porous structure of the  $\text{Co}_3\text{O}_4$  nanoarchitectures, nitrogen adsorption and desorption measurements were performed. Fig. 5 shows the adsorption–desorption isotherm and the corresponding BJH pore size distribution plot (inset in Fig. 5) of the materials. According to the IUPAC classification, the loop observed is ascribed as type H1 loops, and there are abundant pores of 2–50 nm in diameter existing in the materials. Using the BJH method and the desorption branch of the nitrogen isotherm, the calculated size and shape of the pores were not uniform, most of them are around 3.6 nm in diameter (pore volume:  $0.34 \text{ cm}^3 \text{ g}^{-1}$ ) and the average pore diameter is *ca* 15.41 nm in diameter. Porous hierarchical  $\text{Co}_3\text{O}_4$  nanoarchitectures with BET surface area of  $88.34 \text{ m}^2 \text{ g}^{-1}$  have been successfully produced in large scale.

Because the free-standing 3D hierarchical nanostructures could make it easier to establish stable contacts for better electron transportation in the electrochemical electrodes and the high porosity of the materials generated on their surfaces may further offer efficient pathways for ion diffusion, the as-prepared  $\text{Co}_3\text{O}_4$  nanoarchitectures could be ideal candidates suitable for constructing energy storage devices. The electrochemical properties of the materials are therefore evaluated by using them as building blocks to fabricate supercapacitors. Fig. 6a shows the cyclic voltammograms (CV) of the  $\text{Co}_3\text{O}_4$  nanoarchitectures tested in an aqueous electrolyte of KOH from 0 to 0.5 V (vs. SCE) at scan rates between 5 and  $50 \text{ mV s}^{-1}$ . All of the curves mainly exhibit pseudocapacitance features caused by the fast and reversible faradaic redox reaction of the materials [34]. Two pairs of redox peaks can be clearly observed at scan rate of  $5 \text{ mV s}^{-1}$ , which correspond to

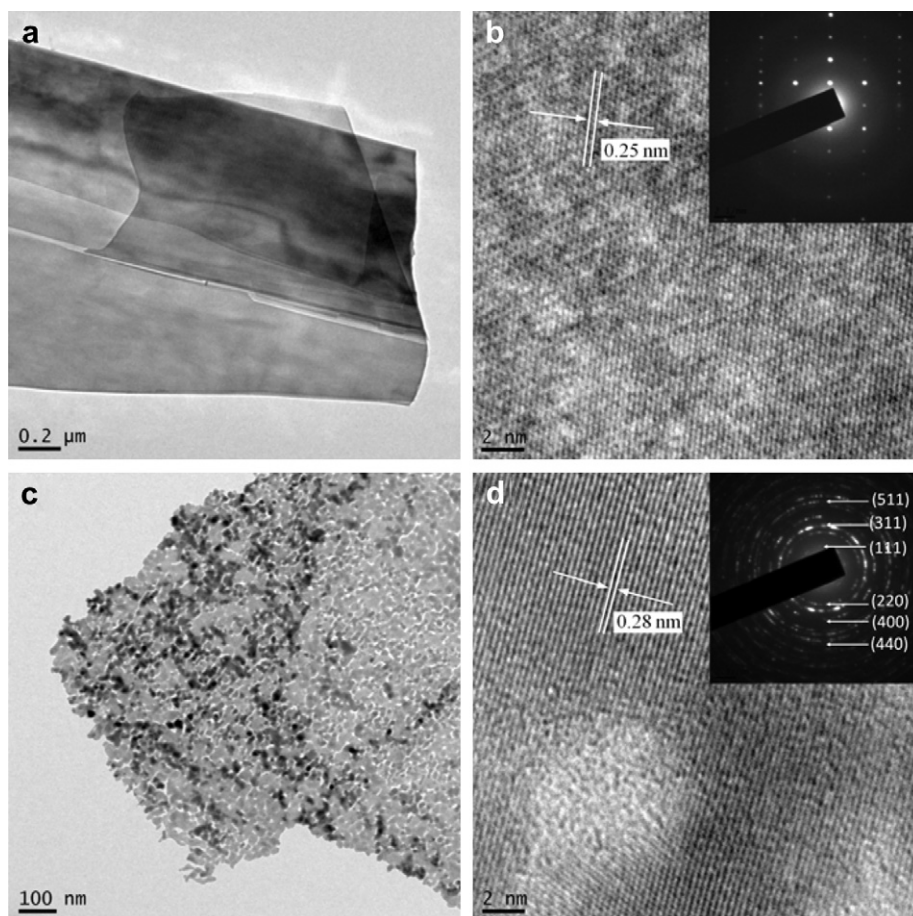


Fig. 4. (a) TEM and (b) HRTEM images of single crystalline  $\text{Co}(\text{CO}_3)_{0.5}(\text{OH}) \cdot 0.11\text{H}_2\text{O}$  nanowall. (c) TEM and (d) HRTEM images of porous  $\text{Co}_3\text{O}_4$  nanowall. Insets in (b) and (d): the SAED patterns of the precursor and the final product.

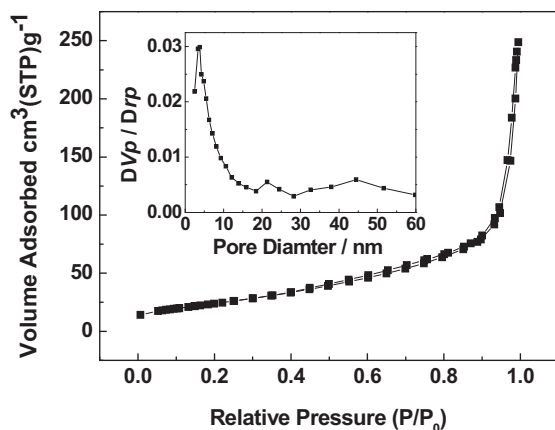
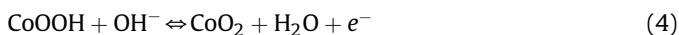
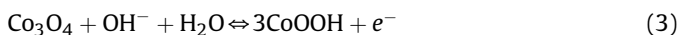


Fig. 5. Typical nitrogen adsorption-desorption isotherm and pore-size distribution curve (inset) of porous  $\text{Co}_3\text{O}_4$  nanoarchitectures.

the conversion between different oxidation states of cobalt according to the following equations (Eq. (3) and (4)) [53]:



In accompanying with the increase of scan rate, the anodic peaks shift toward high potential and the cathodic peaks move toward negative potential simultaneously, which could be attributed to the polarization caused by high scan rate. Fig. 6b shows that the cathodic peak current ( $I_{pc}$ ) is in proportion to the square root of the scan rate ( $v^{1/2}$ ). This indicates that the reactions in the system are controlled by the diffusion process [31].

Fig. 7a shows the galvanostatic charge-discharge curves of the supercapacitors made with porous  $\text{Co}_3\text{O}_4$  nanoarchitectures at different charge-discharge current densities within the potential window of  $-0.05$ – $0.35$  V. The specific capacitance values of the devices obtained from the discharge curves are 997, 982, 928, 843 and  $759 \text{ F g}^{-1}$  at the current density of 0.5, 1, 2, 4 and  $8 \text{ A g}^{-1}$ , respectively (Fig. 7b). The decrease of the capacitances (Fig. 7b) in accompanying with the increase of the discharge current density is likely resulted from the increase of potential drop due to the resistance of the materials and the relatively insufficient Faradic redox reaction of the active material under higher discharge current density. The specific capacitance obtained at the slowest scan rate is more close to fully utilizing the active materials of the electrodes. Their specific capacitance of  $843 \text{ F g}^{-1}$  at current density

of  $4 \text{ A g}^{-1}$  is 39.6% higher than that of the supercapacitors constructed with ultralayered  $\text{Co}_3\text{O}_4$  materials reported recently [28]. The energy storage performances of as-prepared hierarchical  $\text{Co}_3\text{O}_4$  nanoarchitectures have been dramatically improved, compared to that of devices made with urchin-like hierarchical  $\text{Co}_3\text{O}_4$  nanostructures ( $536 \text{ F g}^{-1}$  at  $4 \text{ A g}^{-1}$ ) [33]. This could be resulted from the structure difference between our porous  $\text{Co}_3\text{O}_4$  nanoarchitectures and those reported. The as-prepared free-standing nanoarchitectures with lots of pores on their surfaces could be much more feasible for both ion and electron transportations, compared to that of the multi-layered and urchin-like structures. The supercapacitors made with the free-standing and porous  $\text{Co}_3\text{O}_4$  nanoarchitectures thus also exhibit highly enhanced pseudocapacitance performances in comparison with that of the devices made with  $\text{Co}_3\text{O}_4$  nanotubes [40], nanowires [34], nanoneedles [54], as well as mesoporous layered parallel folding nanostructures [27]. The devices also exhibit comparable performances to those made with  $\text{Co}_3\text{O}_4$  nanonets [45,55].

The working stability of energy storage devices is also crucial for their practical applications. We thus further performed the charge/discharge cycling test to examine the long-term cyclability of the devices made with our materials. The galvanostatic curves (Fig. 7c) of the materials at current density of  $4 \text{ A g}^{-1}$  indicates that the charge-discharge process of the electrode is highly reversible. Fig. 7d further presents the cycling performances of the supercapacitors constructed with the porous  $\text{Co}_3\text{O}_4$  nanoarchitectures under current density of  $4 \text{ A g}^{-1}$  within the potential window of  $-0.05$ – $0.35$  V. A small decrease of the specific capacitance can be observed in the first 200 cycles, which could be resulted from the consumption of electrode materials and binder for the redox taking place on the surface of the electrode. The capacitances of the devices remain almost constant after that. The devices can retain approximately 92.3% of their maximum values, after cycled for 1000 times. The results indicate that the free-standing and porous  $\text{Co}_3\text{O}_4$  nanoarchitectures can be utilized as electrode materials with excellent reaction reversibility. The excellent performances both in cyclability and specific capacitance of the supercapacitors could be attributed to the free-standing, porous 3D hierarchical nanostructures and high crystallinity [55,56] of the electrode materials with the advantages of high structure stability, large surface area and nanosized pores for short path lengths of ion diffusion and electron transport.

The electrochemical impedance spectroscopy (EIS) is a non-destructive and useful technique for evaluating the kinetic and mechanistic information of electrode materials. The data in the form of Nyquist plots (Fig. 8a) were collected in various bias potentials. The Nyquist plots consist of two distinct parts. A semi-circle at high-

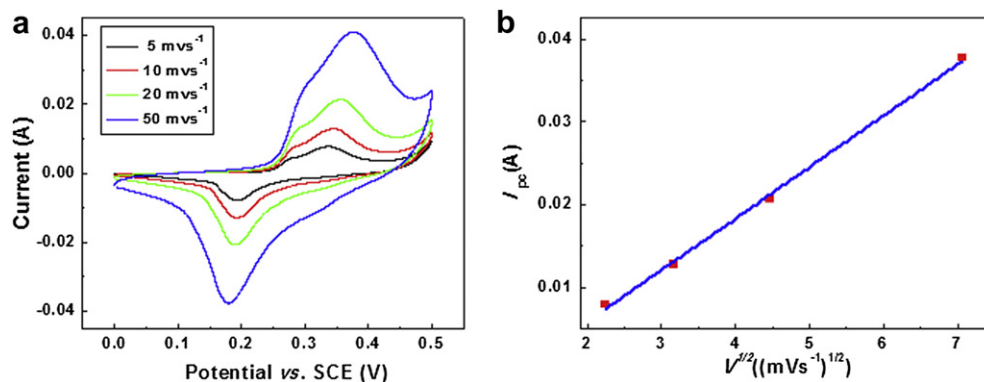
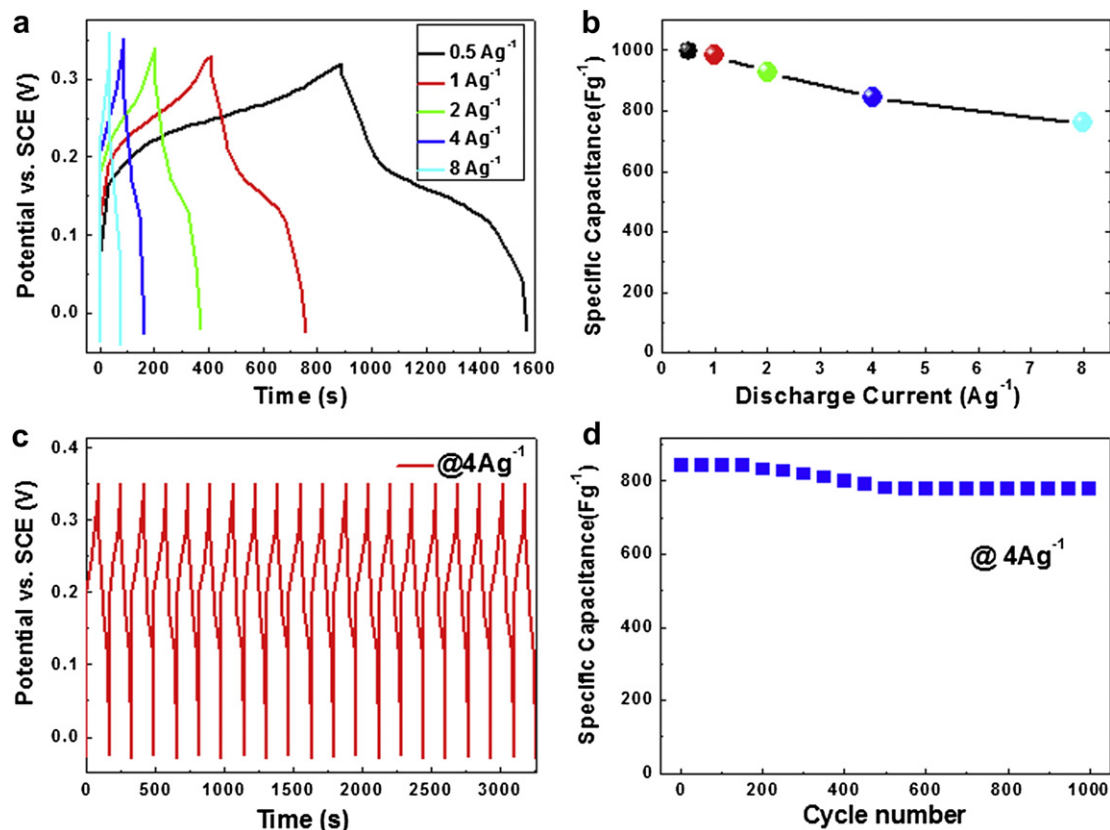
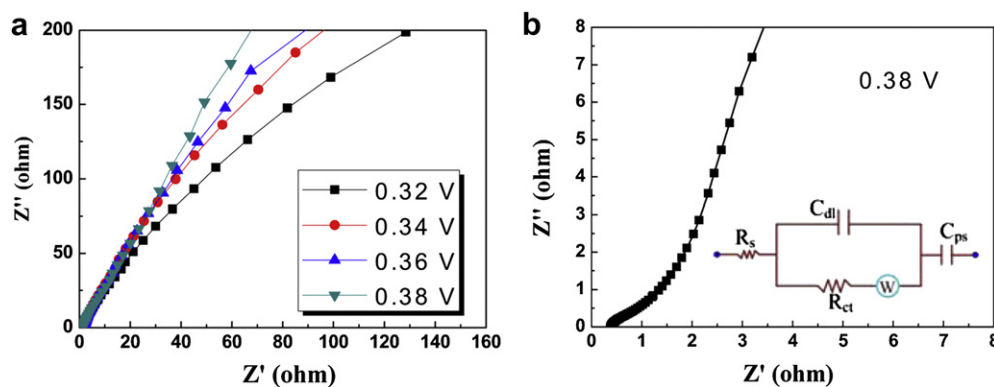


Fig. 6. (a) Cyclic voltammogram of  $\text{Co}_3\text{O}_4$  nanoarchitectures in KOH electrolyte and (b) the relationship between the cathodic peak current ( $I_{pc}$ ) and the square root of the scan rate ( $v^{1/2}$ ).



**Fig. 7.** (a) The charge–discharge curves of the supercapacitors constructed with porous  $\text{Co}_3\text{O}_4$  nanoarchitectures measured at different current densities. (b) Average specific capacitances of the supercapacitors at different discharge current densities. (c) Galvanostatic charge–discharge curves of the devices at current density of 4  $\text{A g}^{-1}$ . (d) Average specific capacitances versus cycle number of the devices at galvanostatic charge and discharge current density of 4  $\text{A g}^{-1}$ .



**Fig. 8.** (a) Nyquist plots of the electrodes made with  $\text{Co}_3\text{O}_4$  nanoarchitectures at different bias potentials and (b) the equivalent circuit diagram of the  $\text{Co}_3\text{O}_4$  electrode from the EIS analysis at bias potential of 0.38 V.

frequency is related to Faradic reactions, and a linear line at low-frequency shows a Warburg impedance related to the diffusion of electrolyte within the pores of the electrode. The equivalent circuit for the impedance analysis is shown in Fig. 8b. Where,  $R_s$  and  $R_{ct}$  represents solution and charge-transfer resistances, respectively.  $C_{dl}$  and  $C_{ps}$  in the circuit are double layer and pseudocapacitance, respectively. The interfacial diffusive resistance (Warburg impedance) in the process has been designated as “W”. In accompanying with increasing the applied potential, there is a gradual change in the linearity of the Nyquist plots, which display the biggest slope of  $72^\circ$  at 0.38 V in the low frequency region. These results suggest that the electrochemical capacitive behavior of the porous  $\text{Co}_3\text{O}_4$  nanoarchitectures is not controlled by diffusion process and the

nanoarchitectures electrode can facilitate ionic motion in solid electrode [40]. In addition, the deviation of linearity along the imaginary axis at different applied potentials is attributed to the pseudocapacitance,  $C_{ps}$ , due to facile and reversible Faradaic redox reactions and accession of the  $\text{OH}^-$  ions into the porous  $\text{Co}_3\text{O}_4$  nanoarchitectures electrode under such low frequencies [28].

#### 4. Conclusions

In summary, a versatile solvothermal synthesis route combined with subsequent calcining process was successfully developed for fabricating free-standing and porous hierarchical  $\text{Co}_3\text{O}_4$  nanoarchitectures in large scale. The electrochemical measurements of

the materials indicate that they exhibit excellent pseudocapacitive performances with specific capacitances of 997 and 759 F g<sup>-1</sup> at 0.5 and 8 A g<sup>-1</sup>, respectively. The supercapacitors constructed also show high stability. The enhanced electrochemical performances of the devices could be attributed to the free-standing and porous 3D hierarchical structure of the materials for their large surface area and porosity favoring transportations both of electrons and electrolytes. Compared to the Co<sub>3</sub>O<sub>4</sub> nanocrystals reported in literature so far, the novelties of this work include: (1) Novel hierarchical Co<sub>3</sub>O<sub>4</sub> nanoarchitectures consisting of nanowalls have been successfully synthesized in large scale for the first time; (2) porous Co<sub>3</sub>O<sub>4</sub> electrode materials can be generated by releasing H<sub>2</sub>O and CO<sub>2</sub> from the precursor with hierarchical nanostructure; and (3) the supercapacitors constructed with hierarchical Co<sub>3</sub>O<sub>4</sub> nanoarchitectures show excellent performances superior to most of the devices fabricated with Co<sub>3</sub>O<sub>4</sub> electrode materials to date. The experimental results indicate that the 3D hierarchical Co<sub>3</sub>O<sub>4</sub> nanoarchitectures consisting of nanowalls with high porosity are promising candidates in designing energy storage devices. The performances of supercapacitors could be further improved through carefully optimizing the microstructures of electrode materials including their porosity and dimensions.

## Acknowledgments

The authors are grateful to the financial support from the National Natural Science Foundation of China (NSFC. 21071130), Outstanding Scholar Program of Henan Province (114200510012), and Program for Advanced Science and Technology of Henan Province (92102310334).

## References

- [1] D.R. Rolison, R.W. Long, J.C. Lytle, A.E. Fischer, C.P. Rhodes, T.M. McEvoy, M.E. Bourga, A.M. Lubers, *Chem. Soc. Rev.* 38 (2009) 226.
- [2] P. Simon, Y. Gogotsi, *Nat. Mater.* 7 (2008) 845.
- [3] J.R. Miller, P. Simon, *Science* 321 (2008) 651.
- [4] E. Frackowiak, F. Beguin, *Carbon* 39 (2001) 937.
- [5] K. Xie, X. Qin, X. Wang, Y. Wang, H. Tao, Q. Wu, L. Yang, Z. Hu, *Adv. Mater.* 24 (2012) 347.
- [6] L.Q. Mai, F. Yang, Y.L. Zhao, X. Xu, L. Xu, Y.Z. Luo, *Nat. Commun.* 2 (2011) 381.
- [7] C. Liu, F. Li, L.P. Ma, H.M. Cheng, *Adv. Mater.* 22 (2010) E28.
- [8] A.S. Arico, P. Bruce, B. Scrosati, J.M. Tarascon, W. Van Schalkwijk, *Nat. Mater.* 4 (2005) 366.
- [9] T. Brezesinski, J. Wang, S.H. Tolbert, B. Dunn, *Nat. Mater.* 9 (2010) 146.
- [10] C.C. Hu, K.H. Chang, M.C. Lin, Y.T. Wu, *Nano Lett.* 6 (2006) 2690.
- [11] C.C. Hu, W.C. Chen, *Electrochim. Acta* 49 (2004) 3469.
- [12] D.W. Wang, Q.H. Wang, T.M. Wang, *Nanotechnology* 22 (2011) 135604.
- [13] M.S. Song, K.M. Lee, Y.R. Lee, I.Y. Kim, T.W. Kim, J.L. Gunjekar, S.J. Hwang, *J. Phys. Chem. C* 114 (2010) 22134.
- [14] C. Jo, I. Hwang, J. Lee, C.W. Lee, S. Yoon, *J. Phys. Chem. C* 115 (2011) 11880.
- [15] C.Z. Yuan, L. Yang, L.R. Hou, L.F. Shen, F. Zhang, D.K. Li, X.G. Zhang, *J. Mater. Chem.* 21 (2011) 18183.
- [16] M.Z. Dai, L.Y. Song, J.T. LaBelle, B.D. Vogt, *Chem. Mater.* 23 (2011) 2869.
- [17] Y.Y. Liang, M.G. Schwab, L.J. Zhi, E. Mugnaioli, U. Kolb, X.L. Feng, K. Mullen, *J. Am. Chem. Soc.* 132 (2010) 15030.
- [18] J.P. Liu, J. Jiang, C.W. Cheng, H.X. Li, J.X. Zhang, H. Gong, H.J. Fan, *Adv. Mater.* 23 (2011) 2076.
- [19] Y.H. Li, K.L. Huang, D.M. Zeng, S.Q. Liu, Z.F. Yao, *J. Solid State Electrochem.* 14 (2010) 1205.
- [20] Y. Xiao, S. Liu, S. Fang, D. Jia, H. Su, W. Zhou, J.B. Wiley, F. Li, *RSC Adv.* 2 (2012) 3496.
- [21] G.L. Wang, D.X. Cao, C.L. Yin, Y.Y. Gao, J.L. Yin, L. Cheng, *Chem. Mater.* 21 (2009) 5112.
- [22] Y. Ding, Y. Wang, L.A. Su, M. Bellagamba, H. Zhang, Y. Lei, *Biosens. Bioelectron.* 26 (2010) 542.
- [23] T. Yu, Y.W. Zhu, X.J. Xu, Z.X. Shen, P. Chen, C.T. Lim, J.T.L. Thong, C.H. Sow, *Adv. Mater.* 17 (2005) 1595.
- [24] X. Wang, X.L. Wu, Y.G. Guo, Y.T. Zhong, X.Q. Cao, Y. Ma, J.N. Yao, *Adv. Funct. Mater.* 20 (2010) 1680.
- [25] X.H. Xia, J.P. Tu, Y.J. Mai, X.L. Wang, C.D. Gu, X.B. Zhao, *J. Mater. Chem.* 21 (2011) 9319.
- [26] J.B. Wu, Y. Lin, X.H. Xia, J.Y. Xu, Q.Y. Shi, *Electrochim. Acta* 56 (2011) 7163.
- [27] D.W. Wang, Q.H. Wang, T.M. Wang, *Inorg. Chem.* 50 (2011) 6482.
- [28] S.K. Meher, G.R. Rao, *J. Phys. Chem. C* 115 (2011) 15646.
- [29] S.K. Meher, G.R. Rao, *J. Phys. Chem. C* 115 (2011) 25543.
- [30] Y.H. Li, K.L. Huang, Z.F. Yao, S.Q. Liu, X.X. Qing, *Electrochim. Acta* 56 (2011) 2140.
- [31] Y.H. Li, K.L. Huang, S.Q. Liu, Z.F. Yao, S.X. Zhuang, *J. Solid State Electrochem.* 15 (2011) 587.
- [32] S.G. Kandalkar, H.M. Lee, H. Chae, C.K. Kim, *Mater. Res. Bull.* 46 (2011) 48.
- [33] L.R. Hou, C.Z. Yuan, L. Yang, L.F. Shen, F. Zhang, X.G. Zhang, *RSC Adv.* 1 (2011) 1521.
- [34] Y.Y. Gao, S.L. Chen, D.X. Cao, G.L. Wang, J.L. Yin, *J. Power Sources* 195 (2010) 1757.
- [35] M.B. Zheng, J. Cao, S.T. Liao, J.S. Liu, H.Q. Chen, Y. Zhao, W.J. Dai, G.B. Ji, J.M. Cao, J. Tao, *J. Phys. Chem. C* 113 (2009) 3887.
- [36] T.Y. Wei, C.H. Chen, K.H. Chang, S.Y. Lu, C.C. Hu, *Chem. Mater.* 21 (2009) 3228.
- [37] P.J. Hall, M. Mirzaei, S.I. Fletcher, F.B. Sillars, A.J.R. Rennie, G.O. Shitta-Bey, G. Wilson, A. Cruden, R. Carter, *Energy Environ. Sci.* 3 (2010) 1238.
- [38] J. Chmiola, C. Largeot, P.L. Taberna, P. Simon, Y. Gogotsi, *Science* 328 (2010) 480.
- [39] E. Hosono, S. Fujihara, I. Honma, H.S. Zhou, *J. Mater. Chem.* 15 (2005) 1938.
- [40] J.A. Xu, L. Gao, J.Y. Cao, W.C. Wang, Z.D. Chen, *Electrochim. Acta* 56 (2010) 732.
- [41] T. He, D.R. Chen, X.L. Jiao, Y.L. Wang, *Adv. Mater.* 18 (2006) 1078.
- [42] S. Xiong, C. Yuan, X. Zhang, B. Xi, Y. Qian, *Chem. Eur. J.* 15 (2009) 5320.
- [43] Y. Xiao, S. Liu, F. Li, A. Zhang, J. Zhao, S. Fang, D. Jia, *Adv. Funct. Mater.* (in press).
- [44] X.H. Xia, J.P. Tu, X.L. Wang, C.D. Gu, X.B. Zhao, *Chem. Commun.* 47 (2011) 5786.
- [45] Y. Fan, H. Shao, J. Wang, L. Liu, J. Zhang, C. Cao, *Chem. Commun.* 47 (2011) 3469.
- [46] H. Liang, J.M. Raitano, L. Zhang, S.-W. Chan, *Chem. Commun.* 48 (2009) 7569.
- [47] L. Chen, J. Hu, R. Richards, S. Prikhodko, S. Kodambaka, *Nanoscale* 2 (2010) 1657.
- [48] O.J. Zhu, Z. Gui, *Mater. Chem. Phys.* 118 (2009) 243.
- [49] H.T. Wang, L. Zhang, X.H. Tan, C.M.B. Holt, B. Zahir, B.C. Olsen, D. Mitlin, *J. Phys. Chem. C* 115 (2011) 17599.
- [50] L. Yang, S. Cheng, Y. Ding, X. Zhu, Z.L. Wang, M. Liu, *Nano Lett.* 12 (2012) 321.
- [51] C.C. Hu, K.H. Chang, T.Y. Hsu, *J. Electrochem. Soc.* 155 (2008) F196.
- [52] T.Y. Wei, C.H. Chen, H.C. Chien, S.-Y. Lu, C.C. Hu, *Adv. Mater.* 22 (2010) 347.
- [53] Y. Wang, H.J. Zhang, J. Wei, C.C. Wong, J.Y. Lin, A. Borgna, *Energy Environ. Sci.* 4 (2011) 1845.
- [54] T. Zhu, J.S. Chen, X.W. Lou, *J. Mater. Chem.* 20 (2010) 7015.
- [55] K.H. Chang, C.C. Hu, *Appl. Phys. Lett.* 88 (2006) 193102.
- [56] C.C. Hu, C.Y. Hung, K.H. Chang, Y.L. Yang, *J. Power Sources* 196 (2011) 847.